Angular Dependency Model for the Meteosat Longwave Radiation

N. Clerbaux, S. Dewitte, C. Bertrand, D. Caprion,

B. De Paepe, L. Gonzalez, A. Ipe

Royal Meteorological Institute of Belgium, http://gerb.oma.be

Abstract

The paper presents the longwave radiance–to–flux conversion which has been developped, implemented and is currently applied to produce the Geostationary Earth Radiation Budget (GERB) Edition-1 thermal flux data. The method is based on theoretical regressions that link the anisotropic factor to the narrowband radiances measured in the SEVIRI thermal channels. The radiative transfer computations used to derive the regressions are described. Cross-comparisons of with the CERES thermal flux indicates an underestimation of the limb–darkening in case of semi–transparent high clouds (cirrus). It is shown that this problem can be in part solved by using a specific regression for this kind of cloudiness. This work indicates a way to improve the quality of the GERB thermal flux in subsequent Editions of the GERB dataset.

Key words: Earth Radiation Budget, Geostationary, Remote sensing, radiance-to-flux conversion, angular distribution model

1 Introduction

Accurate measurement of the Outgoing Longwave Radiation (OLR) is of prime importance to improve our understanding of the climate system. The human activities are modifying the CO_2 concentration in the atmosphere which in turn is modifying the water vapour concentration and the cloudiness. All this is directly affecting the way the Earth is losing energy at the Top Of Atmosphere (TOA) by longwave thermal emission. Over the Meteosat field of view, accurate measurements of the longwave broadband radiance are now available either directly from the Geostationary Earth Radiation Budget (GERB)[*Harries et al.*, 2005] instrument or, indirectly, from the narrowband measurements of the SEVIRI instrument. However, angular modeling of the radiation field is still needed to estimate the flux from the single directional measurement. At this level the geostationary orbit is known to be an inconvenient as any angular modeling error is introducing regional biases in the OLR. Indeed, from the geostationary orbit, a given region of the Earth is always observed with the same viewing geometry. To give an example, from its geostationary orbit, the GERB instrument will always observe the South faces of the Northern hemisphere mountains and the opposite for the Southern hemisphere. In this example, regional error with magnitude of up to 2% are observed [*Clerbaux et al.*, 2003b].

This paper presents the longwave angular modeling which has been developped, implemented and is currently used to produce the GERB Edition-1 dataset. The general methodology of the work is well established and has been widely used: the limb–darkening is modelized using regressions on the narrowband measurements of a multispectral infrared imager. The regression coefficients are derived as best fit on database of radiative transfer computations. Among many others, similar approach is followed by *Schmetz and Liu* [1988] for the Meteosat first generation instrument, *Ellingson et al.* [1989] for the HIRS or by *Stubenrauch et al.* [1993] for ScaRaB.

In the frame of the GERB project, a comprehensive validation of the Edition-1 thermal flux has been carried out and some limitations of the angular modeling have been identified. The main source of angular conversion error is related to the inaccurate modeling of the semitransparent high clouds (*cirrus*). A specific regression is then proposed to improve the cirrus radiance–to–flux conversion for a future second Edition of the GERB dataset. The MPEF OLR (computation recipe pfrom the EUMETSAT web site) is also affected by an underestimation of the TOA anisotropy, with an even higher magnitude than for GERB.

The paper is structured as follows. The next section described the radiative transfer computations over which the regressions are fitted. Then, the section §3 details the angular modeling used to estimate the Edition–1 OLR. Section §4 presents a possible improvement of this modeling for semi–transparent high clouds. Finally, Section §5 summarizes the main results of intercomparisons between the GERB Edition–1 OLR and the same quantity inferred from CERES observation from different viewing geometries.

2 Radiative transfer computations

A large database of TOA spectral radiance fields $L(VZA, \lambda)$ was built using the *Santa Barbara DISORT Atmospheric Radiative Transfer* (SBDART) model [*Ricchiazzi*, 1998]. The simulations are performed for 4622 realistic conditions of the Earth–atmosphere system, as described in *Clerbaux et al.* [2003]. The database is available from the RMIB GERB team web site [1].

The atmospheric profile is from far the main input for the radiative transfer computations in the thermal part of the spectrum. For the simulations, the profiles from the TIGR–3 database [*Chevallier et al.*, 2000] have been used. This data has been kindly made available by the French Laboratoire de Meteorologie Dynamique (LMD). The profiles provide, at 40 pressure levels $(1013, 955, ..., 0.05hPa)$, the temperature as well as thewater vapour and ozone concentrations.

For each of the simulation, the surface skin temperature is set randomly and with an uniform distribution of probability between $[T_0 - 15K$ and $T_0 + 15K$ where T_0 is the temperature in the lower level of the atmospheric profile. This aims to account for the radiative heating or cooling of the surface. However, in some day–time situations, much higher difference between surface and air temperature are observed, as for example over clear desert at the beginning of the afternoon. To simulate this, for 40% of the simulations, the surface skin temperature is set randomly and with an uniform distribution of probability between T_0 and T_0+$50K$. The surface emissivity ϵ must also be specified for the simulations. Ideally, this emissivity should be spectraly dependent $\epsilon(\lambda)$ but, unfortunately, realistic curves $\epsilon(\lambda)$ defined over the $[2.5 - 100]$ μm interval are not yet available. Spectraly unvariant emissivity is then used and set randomly with an uniform distribution of probability between 0.85 and 1.

Realistic cloud covers should also be simulated. This is done for half of the

[1] http://gerb.oma.be/SpectralRadiancesDB/

simulations, the other half being cloud free. The cloudiness can consist of up to 3 different overlapping cloud layers. The characteristics of these layers are independent one to the others. The lower cloud layer is simulated with a probability of 50%, is located at a height between $500m$ and $3500m$ (uniform distribution of probability), and is always constituted of water droplets. The probability of middle level cloud is 40%, the layer is located between $4000m$ and $7000m$ and is constituted of ice particles in 25% of the cases and water droplets in 75% of the cases. The probability of high level cloud is 30%, the layer is located between $7000m$ and $16000m$ and is always constituted of ice particles. For a water phase layer, 2 kinds of clouds are simulated with an equal probability: precipitating and non-precipitating clouds. The effective radius of the droplet size distribution is then chosen randomly and with an uniform distribution of probability within $[2 : 25]$ μm for non-precipitating clouds and $[25 : 128]$ μm for precipitating clouds. For a ice phase layer, the single scattering co–albedo $(1 - a)$ predicted using the Mie theory, is modified by a multiplicative factor chosen randomly in the range $[0.5 : 1]$, as suggested by *Ricchiazzi et al.* [1998]. The single scattering co–albedo is the ratio between the probability of absorption and the probability of scattering. Finally, the optical thickness of the cloud layers should be specified. The type is selected randomly with an equal probability between : thin, medium and thick layer. The optical thickness is then selected randomly within [0 : 3.6] (thin), [3.6 : 23] (medium) and [23 : 379] (thick). These values are chosen to match the ISCCP cloud classification.

No stratospheric aerosol are added in the simulations. The type of boundary layer aerosol is chose randomly and with an equal probability within: none, rural, urban, oceanic, tropospheric. The SBDART model default parameterization and wavelength dependency are used.

The computations have been done at 431 wavelengths λ covering the thermal region $[2.5 - 100]$ μm. (the lower and upper limits for SBDART thermal simulation). Between 2.5 μm and 20 μm a walength increment of $\delta\lambda = 0.05\mu$m is used while between 20 μm and 100 μm the increment is $\delta\lambda = 1.0\mu$m, to limit the computation time. The spectral radiance curves $L(\lambda)$ are then extended up to 500μm using the planck's law with brightness temperature given by the radiative transfer model at 100μm. All the simulations are done with the incoming solar radiation turned off in order to simulate only the radiation due to the planetary thermal emission. For each wavelength and each simulation, the spectral flux $F(\lambda)$ is computed as well as the spectral radiance field with a 5° resolution in viewing zenith angle ($VZA = 0°, 5°, 10°, ..., 85°$).

Being a *plane–parallel* radiative transfer model, SBDART can not simulate neither the anisotropy due to structured surfaces [*Otterman et al.*, 1997] nor the anisotropy due to broken cloud fields [*Duvel et al.*, 1984]. On the other hand, the database is representative of the anisotropy due to surface temperature, atmospheric constituent profiles and due to stratiform cloud covers, including the strong anisotropy due to semi–transparent high clouds (*cirrus*).

For each element in the database, the broadband (BB) flux F, the BB radiance $L(VZA)$ and the anisotropic factors $R(VZA) = \pi L(VZA)/F$ are evaluated at $VZA = \{0°, 5°, ..., 85°\}$, as well as the narrowband radiances in the 7 SEVIRI thermal channels (the IR 3.9 channel is discarded due to day-time solar contamination). The Fig. (1, top) shows the scatterplot of the anistropic factor at nadir $R(VZA = 0°)$ versus the thermal radiance $L(VZA = 0°)$ for the 4622 simulations. In general the anisotropic factor $R(0°)$ increases more or less linearly with the BB radiance L. This is the effect of the temperature difference between the surface and the atmosphere. As an exception, the strong anisotropy induced by semi–transparent high clouds is clearly visible in the figure. This scatterplot shows that, even using a simple plane–parallel radiative transfer model like SBDART, it is possible to generate radiance fields at the TOA exhibiting large dispersion in term of anisotropy.

3 GERB Edition-1 LW ADM

For the first Edition of the GERB Level 2 dataset, a second order regresssion on the SEVIRI WV 6.2, IR 10.8, IR 12 and IR 13.4 is used to estimate the anisotropic factor

$$\begin{aligned} R = & c_0 + c_1 L_{6.2} + c_2 L_{10.8} + c_3 L_{12} + c_4 L_{13.4} + c_5 L_{6.2}^2 + c_6 L_{10.8} L_{6.2} + \\ & c_7 L_{10.8}^2 + c_8 L_{12} L_{6.2} + c_9 L_{12} L_{10.8} + c_{10} L_{12}^2 + c_{11} L_{13.4} L_{6.2} + \\ & c_{12} L_{13.4} L_{10.8} + c_{13} L_{12} L_{10.8} + c_{14} L_{13.4}^2 \end{aligned} \tag{1}$$

where the narrowband radiances $\{L_{ch}\}$ are expressed in $[Wm^{-2}sr^{-1}]$ unit. The radiances in the WV 7.3, IR 8.7 and IR 9.7 SEVIRI channels have been discarded due to their sensitivity on the surface emissivity ϵ. The IR 3.9 radiance is not used due to day-time solar contamination in this channel. The coefficients $\{c_i\}$ in Eq. (2) are fitted on the database (least mean square minimization) for the different $VZA = 0°, 5°, ..., 85°$. Before the fit, the simulated NB radiances are randomly altered with a gaussian noise having standard deviation equal to 10% of the average radiance in the channel. This is implemented to avoid that the regressions exploit too tiny correlation between the different NB channels. This 10% noise should simulate the effect of SEVIRI

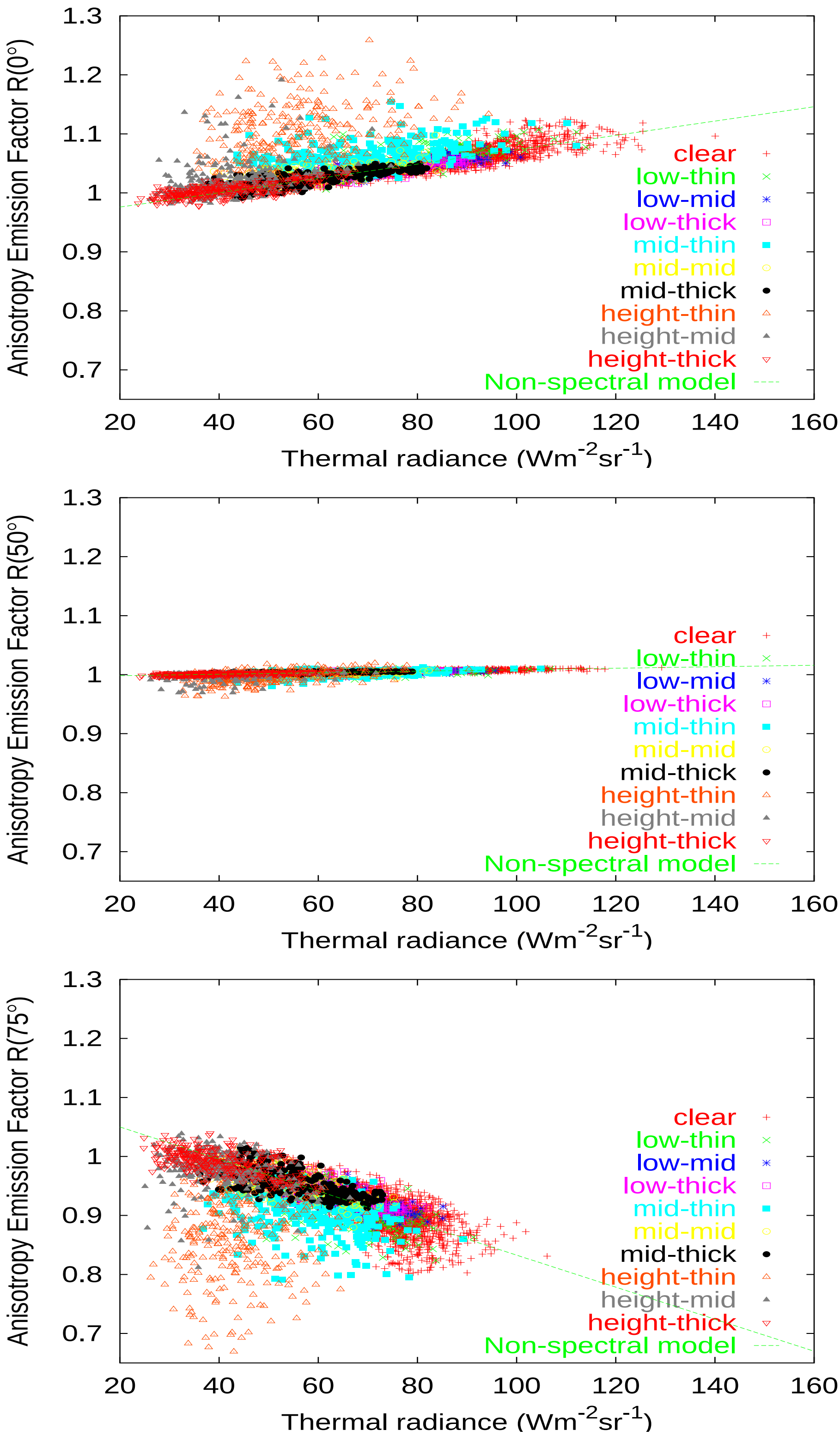

Fig. 1. Scatter plots of the anisotropic factor $R(VZA)$ versus the thermal radiance $L(VZA)$ for 3 angles of observation: $VZA = 0°$ (top), $VZA = 50°$ (center) and $VZA = 75°$ (bottom). The 4622 elements in the database are plotted using the ISCCP cloud classification.

thermal channel calibration (about 2%) and the effect of difference in surface emissivity between the channels ($\sim 8\%$). The Tab.(1) gives the best fit coefficients $\{c_i\}$ valid for the SEVIRI instrument on MSG-1. The coefficients are slightly different for the MSG-2 satellite (not given here).

VZA	c_0	c_1	c_2	c_3	c_4	c_5	c_6	c_7	c_8	c_9	c_{10}	c_{11}	c_{12}	c_{13}	c_{14}
00	0.998249	-0.044502	0.008858	0.008930	0.002318	0.026631	-0.000584	0.001203	-0.001467	-0.001675	0.000225	-0.000559	-0.001387	0.000397	0.000070
05	0.998325	-0.044068	0.008776	0.008841	0.002281	0.026445	-0.000588	0.001193	-0.001440	-0.001661	0.000220	-0.000571	-0.001372	0.000399	0.000068
10	0.998487	-0.042712	0.008533	0.008581	0.002179	0.025869	-0.000595	0.001160	-0.001359	-0.001619	0.000208	-0.000614	-0.001328	0.000406	0.000061
15	0.998620	-0.040335	0.008131	0.008156	0.002021	0.024860	-0.000600	0.001106	-0.001233	-0.001548	0.000187	-0.000696	-0.001254	0.000414	0.000050
20	0.998674	-0.036866	0.007565	0.007569	0.001820	0.023370	-0.000596	0.001028	-0.001067	-0.001444	0.000158	-0.000819	-0.001152	0.000422	0.000037
25	0.998649	-0.032262	0.006822	0.006814	0.001584	0.021348	-0.000578	0.000925	-0.000870	-0.001306	0.000122	-0.000978	-0.001021	0.000424	0.000022
30	0.998471	-0.026391	0.005894	0.005894	0.001330	0.018698	-0.000535	0.000794	-0.000658	-0.001126	0.000082	-0.001172	-0.000862	0.000415	0.000007
35	0.997916	-0.019010	0.004781	0.004823	0.001087	0.015264	-0.000445	0.000634	-0.000459	-0.000900	0.000036	-0.001408	-0.000679	0.000387	-0.000004
40	0.996722	-0.009827	0.003489	0.003620	0.000884	0.010822	-0.000279	0.000442	-0.000312	-0.000621	-0.000013	-0.001686	-0.000479	0.000333	-0.000005
45	0.994715	0.001410	0.002028	0.002293	0.000738	0.005097	-0.000005	0.000217	-0.000276	-0.000281	-0.000064	-0.001971	-0.000276	0.000244	0.000009
50	0.991728	0.014992	0.000429	0.000842	0.000651	-0.002303	0.000408	-0.000042	-0.000435	0.000124	-0.000114	-0.002182	-0.000086	0.000117	0.000045
55	0.987412	0.031319	-0.001235	-0.000732	0.000626	-0.012019	0.000996	-0.000330	-0.000925	0.000591	-0.000157	-0.002146	0.000061	-0.000046	0.000106
60	0.981304	0.050730	-0.002834	-0.002447	0.000658	-0.025104	0.001759	-0.000635	-0.001937	0.001095	-0.000178	-0.001467	0.000125	-0.000235	0.000184
65	0.973284	0.073030	-0.004196	-0.004425	0.000699	-0.043259	0.002549	-0.000934	-0.003705	0.001584	-0.000141	0.000795	0.000071	-0.000432	0.000243
70	0.963868	0.096972	-0.005140	-0.006943	0.000618	-0.069546	0.002767	-0.001191	-0.006398	0.001975	0.000010	0.006773	-0.000113	-0.000629	0.000192
75	0.953590	0.118958	-0.005597	-0.010278	0.000217	-0.110429	0.000668	-0.001403	-0.009767	0.002234	0.000308	0.021374	-0.000338	-0.000908	-0.000180
80	0.942775	0.125563	-0.006335	-0.014274	-0.000496	-0.176132	-0.008374	-0.001688	-0.012324	0.002544	0.000650	0.056482	-0.000138	-0.001590	-0.001463
85	0.936184	0.097418	-0.014125	-0.022277	0.003343	-0.239616	-0.034167	-0.002147	-0.008016	0.003235	0.001026	0.124583	0.002012	-0.002957	-0.005462

Table 1

Coefficients c_i of the regression Eq. (2) to estimate the broadband anisotropic factor R as a function of the SEVIRI on MSG-1 narrowband radiance in the channels WV 6.2, IR 10.8, IR 12 and IR 13.4.

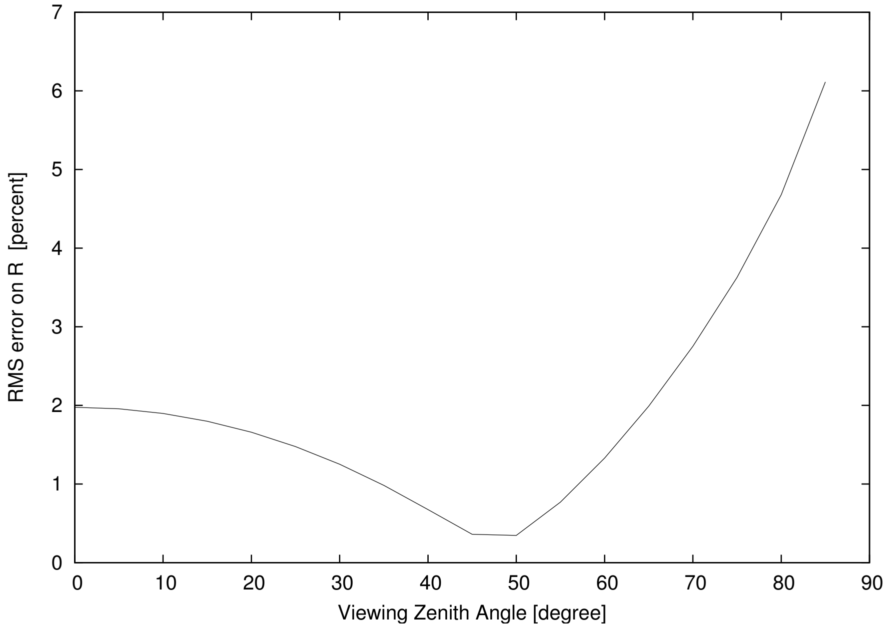

Fig. 2. Residual RMS error [%] of the regression Eq.(2) according to the viewing zenith angle.

The Fig.(2) gives radiance–to–flux conversion error according to the viewing zenith angle. The Figure shows a noticeable minimum for viewing zenith angle close to 50° which is a well-known fact. For nadir view, the LW angular modelling introduces a RMS error of about 2% in term of anisotropic factor. About the half of this error is due to the high semi-transparent clouds, as showed in *Clerbaux et al.* [2003].

4 Cirrus clouds processing

The GERB Edition-1 data exhibits a clear underestimation of the anisotropy in presence of cirrus clouds. Theoretical study indicates that the maximum effect of this kind of cloud on the longwave anisotropy is observed for cloud optical thickness of about $\tau_{0.55\mu m} \sim 1.5$, this value being slightly dependent on the cloud height. The GERB cloud retrieval is not helpful to detect this

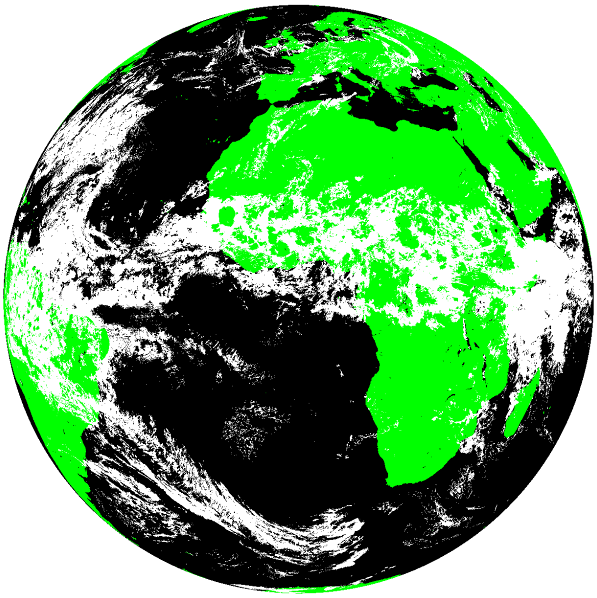

Fig. 3. Illustration of the detection of semi–transparent high cloud (in white) with Eq.(2) for the SEVIRI repeat cycle 200407100000.

kind of clouds, as the cloud retrieval is based on the SEVIRI visibles channels and can then only be applied during day–time. Others cloud retrievals like the EUMETSAT MPEF processing or the Nowcasting SAF cloud products do not provide the cloud optical thickness. We have then used a rough detection of this kind of clouds by analyzing the difference of brightness temperatures in the $10.8\mu m$ and $12\mu m$ channels. The following simple test is used to detect the high semi–transparent clouds

$$\begin{aligned} T_{10.8} &< T_{max} \\ T_{10.8} - T_{12} &> \Delta T_{min} \end{aligned} \tag{2}$$

The thresholds T_{max} and ΔT_{min} are dependent on the VZA and are estimated from the SBDART simulations in such a way that the number of selected clouds is 10% of the total number of cloudy cases. The Fig. (3) illustrates this very simple detection of high semi–transparent clouds.

We have used this criteria to select high semi-transparent clouds in our database of SBDART simulations and to derive a specific regression applicable for this kind of cloudiness. The following very simple anisotropic model is proposed:

$$R = a + b(T_{10.8} - 268K) + c(T_{10.8} - T_{12} - 2.65K) \tag{3}$$

where the regression parameters a, b, c are dependent on the VZA, as for the general model of Eq.(2). The values $268K$ and $2.65K$ are introduced to have the a parameter more or less representative of the anisotropic factor R. The value of the thresholds for Eq.(2) and the best-fit parameters for Eq.(3) are given in Tab.(2).

5 Validations using CERES observations

5.1 The CERES data

The GERB angular modeling is validated by comparison with colocated fluxes provided by the Cloud and the Earth's Radiant Energy System (CERES) [*Wielicki et al.*, 1996] instruments on the Terra and Aqua satellites. Hereafter, we focus on FM3 instruments data for 21–27 June and 11–17 Dec. 2004. The FM3 instrument is operated in the Rotating Azimuth Plane (RAP) scan mode which provides an excellent angular sampling of the radiance field at the TOA. Indeed, a given place on the Earth, which is always observed with the same viewing geometry from from Meteosat, is observed during the CERES overpasses from more or less random angles.

VZA	T_{max}	DT_{min}	a	b	c
00	299.282313	1.615675	1.098666	-0.000317	0.009330
05	299.250155	1.617385	1.097650	-0.000311	0.009314
10	299.104791	1.616820	1.094740	-0.000313	0.009213
15	298.742661	1.629715	1.090615	-0.000334	0.008576
20	298.419897	1.638374	1.084360	-0.000306	0.007736
25	297.796925	1.648752	1.076127	-0.000322	0.006849
30	297.382058	1.648369	1.066005	-0.000305	0.005495
35	296.836573	1.653364	1.053050	-0.000213	0.004210
40	296.534942	1.652370	1.037383	-0.000037	0.002755
45	295.380668	1.654829	1.019367	0.000171	0.001147
50	294.537985	1.663524	0.999512	0.000425	-0.001072
55	293.744438	1.663545	0.977818	0.000715	-0.003765
60	292.766850	1.688397	0.952388	0.001223	-0.005867
65	290.610468	1.717363	0.926658	0.001656	-0.009296
70	289.035410	1.876048	0.903462	0.002000	-0.014420
75	287.241836	2.153261	0.890758	0.001133	-0.023426
80	283.987527	2.665751	0.869622	-0.000863	-0.023848
85	277.608639	3.536088	0.816913	-0.002718	-0.021795

Table 2

Coefficients c_i of the regression Eq. (2) to estimate the broadband anisotropic factor R as a function of the SEVIRI on MSG-1 narrowband radiances in the channels WV 6.2, IR 10.8, IR 12 and IR 13.4.

5.2 Flux bin analysis

The difference between the geostationary thermal flux (which can be GERB–like[2] Ed-1, GERB–like + cirrus processing or MPEF OLR) and the CERES

[2] The GERB–like data are derived from SEVIRI narrowband–to–broadband conversion [*Clerbaux et al.*, 2005] followed with exactly the same radiance–to–flux con-

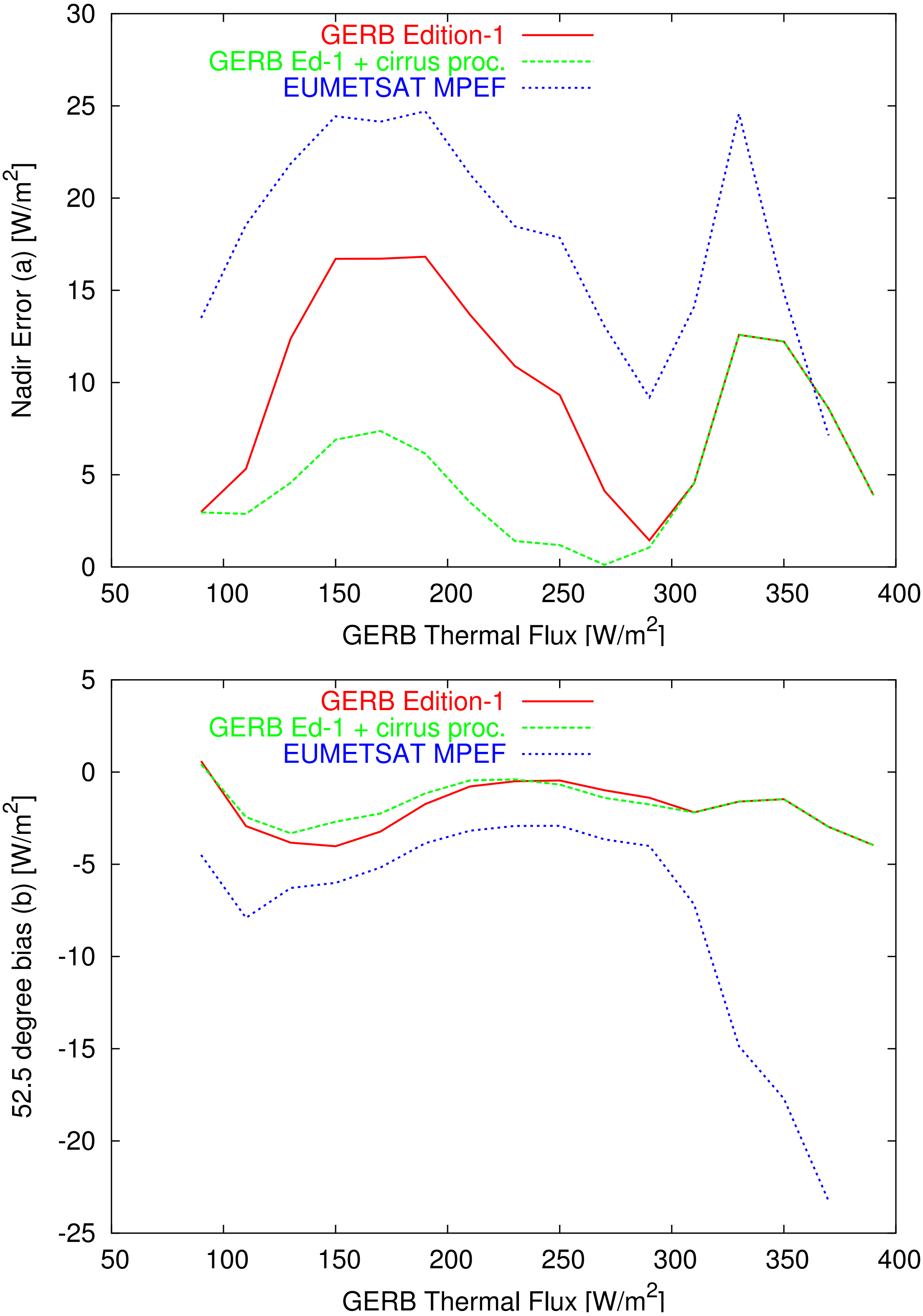

Fig. 4. Angular dependency (parameter a, left) and overall bias (parameter b, right) for the GERB–like Ed-1 dataset (red), the improvement with the cirus processing (green) and the MPEF OLR (blue).

flux is analysed in bins of $20Wm^{-2}$. Then, the difference (GEO - CERES) is fitted as a linear function of the GERB viewing zenith angle VZA:

$$F_{GEO} - F_{CERES} = a(F_{GEO})\frac{52.5 - VZA}{52.5} + b(F_{GEO}) \tag{4}$$

The fit parameter a indicates remaining angular dependency in the radiance–to–flux conversion while the parameter b is symptomatic of the overall offset between the 2 datasets. The Fig. (3) displays the values of these parameters in the $20Wm^{-2}$ bins. In average, the GEO and CERES fluxes are in good agreement. However, the anisotropy is underestimated (positive a value) for cold and for very hot scenes, with maximum anisotropy error located at $\sim 170Wm^{-2}$ and $\sim 330Wm^{-2}$, respectively. The first maximum (up to $16Wm^{-2}$) is introduced by the high anisotropy in case of high semi–transparent clouds. This problem is partly reduced by the dedicated cirrus ADM proposed in §4. The cause of the second maximum is not clear at this time. It can be due to surface emissivity problem over hot desert or to 3–dimensional effects of cloud fields. The MPEF OLR algorithm (blue curve) exhibits the same kind of angular modeling error but with higher underestimation of the anisotropy.

5.3 Regional scale analysis

The Fig. (4) shows the ratio between the GERB Ed-1 and the CERES flux in boxes of 5*5 ARG pixels ($\sim 250km$). The nadir thermal flux overestimation is visible in area of tropical cloudiness and this area follows the seasonal displacement of the ITCZ.

---

version as for the actual GERB data.

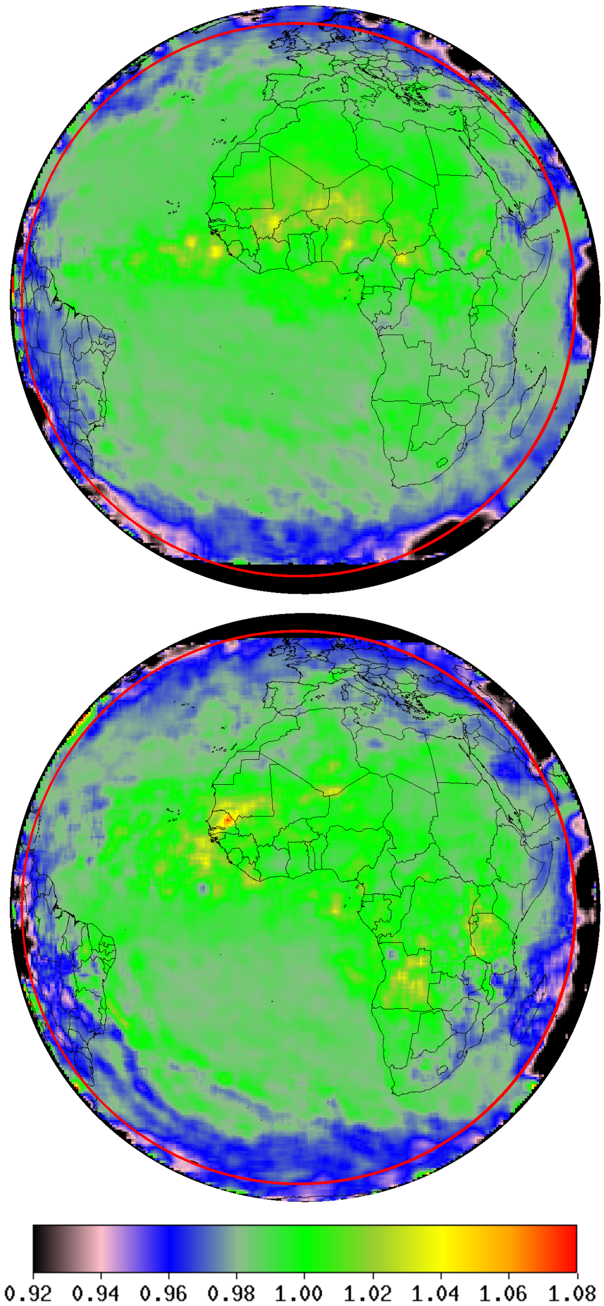

Fig. 5. Day time ratio between GERB Ed1 and CERES FM3 OLR for June (right) and December (left) 2004. The red circle indicates the 70° viewing zenith angle.

6 Conclusions

The validation of the radiance–to–flux conversions is of prime importance when Earth Radiation Budget components are inferred from geostationary observations. At this level, data from the CERES instruments operated in RAP scan mode are very useful as providing a good sampling of all the upper hemisphere directions.

Although the GERB and CERES fluxes agree well in average, the methodology allows the detection of angular dependency problem in the GERB Edition-1 dataset. The main problem concerns semi–transparent high clouds where relative error of up to 20% are introduced during the radiance–to–flux conversion when the radiance is observed at the nadir. This limitation has been included in the GERB Edition-1 Quality Summary document [*Russel*, 2006]. However, this work shows that this problem can be reduced by a better exploitation of the information available in the SEVIRI channels, for example through a specific cirrus angular model.

It is worth to note that similar problem is observed in the OLR derived from Meteosat First Generation data with the scheme of *Schmetz and Liu* [1988]. In this case it is much more difficult to detect cirrus clouds than with MSG (there is only one WV and one IR channel on the first generation of EUMETSAT geostationary satellite) and to apply a cirrus ADM model. However, the Eq.(4) can still be use to correct the OLR in a statistical point of view.

References

[1] Harries, J.E., et al., 2005: The Geostationary Earth Radiation Budget Experiment (GERB), Bulletin of the American Meteorological Society, Vol. 86(7): 945–960.

[2] Chevallier, F. and Chédin, A. and Chéruy, F. and Morcrette, J. J., 2000: TIGR-like atmospheric-profile databases for accurate radiative-flux com-

putation, Quarterly Journal of the Royal Meteorological Society, Vol. 126, 777–785.

[3] Clerbaux, N. and Dewitte, S. and Gonzalez, L. and Bertand, C. and Nicula, B. and Ipe, A., 2003: Outgoing longwave flux estimation improvement of angular modelling using spectral information, Remote Sensing of Environment, Vol. 85(3): 389–395.

[4] Clerbaux, N. and Ipe, A. and Bertrand, C. and Dewitte S.and Nicula, B. and Gonzalez, L., 2003b, Evidence of Azimuthal Anisotropy for the Thermal InfraredRadiation Leaving the Earth's Atmosphere, International Journal for Remote Sensing,24, 3005–3010,

[5] Clerbaux, N. and Bertrand, C. and Caprion, D. and Depaepe, B. and Dewitte, S. and Gonzalez, L. and Ipe, A., 2005: Narrowband-to-broadband Conversions for SEVIRI, Proc. of the 2005 EUMETSAT Meteorological Satellite Conference, pages 351–357.

[6] Duvel, J. P. and Kandel, R. S., 1984: Anisotropy of Longwave Radiation Emergent from a Broken Cloud Field andits Effect on Satellite Estimates of Flux, Journal of Climate and Applied Meteorology, 23, 1411–1420.

[7] Ellingson, R. and Yanuk, D. and Lee, H-T. and Gruber, A., 1989: A Technique for Estimating Outgoing Longwave Radiation from HIRS Radiance Observations, Journal of Atmospheric and Oceanic Technology, 6, 706–711.

[8] Otterman, J. and Starr, D. and Brakke, T. and Davies, R. and Jacobowitz, H. and Mehta, A. and Chéruy, F. and Prabhakara, C., 1997: Modeling Zenith-Angle Dependence of Outgoing Longwave Radiation: Implication for Flux measurements, Remote Sensing of Environment, 62, 90–100.

[9] Ricchiazzi, P. and Yang, S. and Gautier, C. and Sowle, D., 1998: SBDART: A Research and Teaching Software Tool for Plane-Parallel Radiative Transfer in the Earth's Atmosphere, Bulletin of the American Meteorological

Society, 79, 2101–2114.

[10] Russel, J., 2006: Quality Summary for the GERB Edition-1 L2 ARG products. Available at
ftp://gerb.oma.be/Documents/GERBED1_ARG_QS.pdf

[11] Schmetz, J. and Liu, Q., 1988: Outgoing longwave radiation and its diurnal variation at regional scales derived from METEOSAT, Journal of Geophysical Research. Vol. 93 (D9): 11192–11204.

[12] Stubenrauch, C.J. and Duvel, J.P. and Kandel, R.S., 1993: Determination of Longwave Anisotropic Emission Factors from Combined Broad- and Narrowband Radiance Measurements, Journal of Applied Meteorology, Vol. 32, 848–856.

[13] Wielicki, B. A., et al., 1996: Clouds and the Earth's Radiant Energy System (CERES): An Earth Observing System Experiment, Bulletin of the American Meteorological Society, Vol. 77: 853–868.

Acknowledgment

We are grateful to the Atmospheric Sciences Data Center at NASA Langley Research Center for providing the CERES data used in this study.